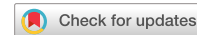


communications

earth & environment

ARTICLE



<https://doi.org/10.1038/s43247-023-00873-8>

OPEN

Multi-proxy validation of glacial-interglacial rainfall variations in southwest Sulawesi

Alena K. Kimbrough^{1,2}✉, Michael K. Gagan^{1,2,3}, Gavin B. Dunbar⁴, Wahyoe S. Hantoro^{2,5}, Chuan-Chou Shen^{6,7}, Hsun-Ming Hu^{6,7}, Hai Cheng^{8,9}, R. Lawrence Edwards¹⁰, Hamdi Rifai¹¹ & Bambang W. Suwargadi⁵

Speleothem $\delta^{18}\text{O}$ is widely used as a proxy for rainfall amount in the tropics on glacial-interglacial to interannual scales. However, uncertainties in the interpretation of this renowned proxy pose a vexing problem in tropical paleoclimatology. Here, we present paired multi-proxy geochemical measurements for stalagmites from southwest Sulawesi, Indonesia, and confirm changes in rainfall amount across ice age terminations. Collectively, the stalagmites span two glacial-interglacial transitions from ~380,000 to 330,000 and 230,000 to 170,000 years ago. Mg/Ca in the slow-growing stalagmites is affected by water moving through the karst and prior calcite precipitation, making it a good proxy for changes in local rainfall. When paired, Mg/Ca and $\delta^{18}\text{O}$ corroborate prominent shifts from drier glacials to wetter interglacials in the core of the Australasian monsoon domain. These shifts in rainfall occur 4,000–7,000 years later than glacial-interglacial increases in global temperature and the associated response of Sulawesi vegetation, determined by speleothem $\delta^{13}\text{C}$.

¹ Research School of Earth Sciences, The Australian National University, Acton, ACT 2601, Australia. ² School of Earth, Atmospheric and Life Sciences, University of Wollongong, Wollongong, NSW 2522, Australia. ³ School of Earth and Environmental Sciences, The University of Queensland, St. Lucia, QLD 4072, Australia. ⁴ Antarctic Research Centre, Victoria University of Wellington, Wellington 6140, New Zealand. ⁵ Research Center for Geotechnology, Indonesian Institute of Sciences, Bandung 40135, Indonesia. ⁶ High-Precision Mass Spectrometry and Environment Change Laboratory (HISPEC), Department of Geosciences, National Taiwan University, Taipei 10617, Taiwan, ROC. ⁷ Research Center for Future Earth, National Taiwan University, Taipei 10617, Taiwan, ROC. ⁸ Institute of Global Environmental Change, Xi'an Jiaotong University, 710054 Xi'an, China. ⁹ Key Laboratory of Karst Dynamics, MLR, Institute of Karst Geology, CAGS, 541004 Guilin, China. ¹⁰ Department of Earth and Environmental Sciences, University of Minnesota, Minneapolis, MN 55455, USA. ¹¹ Department of Physics, Universitas Negeri Padang, Padang 25131, Indonesia. ✉email: akimbrough@uow.edu.au

A basic understanding of the timing and magnitude of natural variability of tropical rainfall in the past is critical to place present trends in context and to validate climate model performance¹. Much of modern society directly or indirectly relies on the consistency of seasonal rains for agriculture in tropical monsoon settings^{2,3}. Reliable and well-constrained hydroclimate records from the tropics, and from the heavily populated Australasian monsoon domain in particular, are necessary for understanding processes driving monsoon strength and deep convection over the Indo-Pacific Warm Pool over multiple timescales. While ice cores, lake sediments, and tree-rings make up a large proportion of terrestrial paleoclimate records at the higher latitudes, speleothems provide exceptionally long, highly resolved and well-dated land-based archives of glacial–interglacial (G–I) rainfall variability at tropical latitudes^{4–13}. At present, over 350 speleothem $\delta^{18}\text{O}$ records have been published for monsoon domains in Australasia and the Americas¹⁴ (Fig. 1).

Early speleothem $\delta^{18}\text{O}$ records for the core area of the Australasian monsoon were generally interpreted to reflect rainfall amount and relevant moisture sources (e.g., summer monsoon intensity and El Niño Southern Oscillation), consistent with the amount effect^{7,9,15,16}. As the number of paleoclimate records for near-equatorial monsoonal settings continues to grow, alongside ongoing monitoring programmes and climate modelling, it is clear that speleothem $\delta^{18}\text{O}$ and rainfall $\delta^{18}\text{O}$ in these areas are influenced by site-specific factors and integrated changes in atmospheric circulation that may not always reflect rainfall amount^{17–22}. Therefore, in tropical monsoon settings, the ideal situation would be to utilise a multi-proxy approach capable of separating the amount effect from rainfall $\delta^{18}\text{O}$ influenced by source moisture and oxygen-isotope fractionation along transport pathways. A better understanding of the utility of speleothem $\delta^{18}\text{O}$, by far the most commonly used proxy for paleomonsoon reconstructions, will improve our ability to identify the drivers of past monsoon rainfall variability. Glacial–interglacial transitions provide an opportunity to understand how globally significant monsoon systems respond to periods of rapid warming. Information gained from tropical speleothem $\delta^{18}\text{O}$ combined with proxies sensitive to local rainfall can assist in attributing major changes in rainfall amount to a particular shift in the regional hydrological system.

Tandem measurements of speleothem Mg/Ca and $\delta^{18}\text{O}$ offer the possibility of decoupling local rainfall amount from variations in rainfall $\delta^{18}\text{O}$ due to changes in regional atmospheric circulation and moisture source^{4,23–25}. Prior calcite precipitation (PCP) is recognised as a primary control on speleothem Mg/Ca variability and is controlled by effective infiltration (i.e., karst infiltration rate and local rainfall amount)^{26,27} and by the pCO₂ content of cave air^{28–30}. During periods of reduced rainfall, the infiltration rate is reduced, and water remains in the karst zone for extended periods. These conditions can cause increased void space in the karst and CO₂ degassing from seepage waters, which enhances the likelihood of calcite precipitating along flow pathways prior to the dripwater reaching a stalagmite^{26,31}. The pCO₂ content of the air in the cave and void spaces drives the degassing process and is influenced by soil pCO₂, atmospheric pCO₂, and cave ventilation^{30,32}. Since calcite precipitation discriminates against both Mg and Sr in favour of Ca (i.e., Mg and Sr partition coefficients are less than one²⁶), PCP causes Mg/Ca and Sr/Ca in seepage waters upstream of the stalagmite to increase. Mg/Ca and Sr/Ca ultimately precipitated on the stalagmite will be elevated accordingly. The preference for Ca to precipitate out of solution during PCP drives coherency among stalagmite Mg/Ca and Sr/Ca and the slope of the ln(Sr/Ca) versus ln(Mg/Ca) regression line can serve as a test for the occurrence of PCP^{33–35}. As speleothem

$\delta^{13}\text{C}$ has been shown to record changes in vegetation and soil pCO₂^{36,37}, comparison with speleothem $\delta^{13}\text{C}$ can further distinguish primary environmental or climatic signals preserved in each proxy. Given the complexity of these interconnected processes, it is optimal to use multiple speleothems and a multi-proxy approach to produce accurate palaeohydrological records.

Few studies have reported on paired records of $\delta^{18}\text{O}$, $\delta^{13}\text{C}$, and trace elements for speleothems that span multiple G–I cycles^{4,24,38}. Our study site in southwest Sulawesi, Indonesia, located in the core area of the Australasian monsoon, is ideally positioned to test the utility of speleothem $\delta^{18}\text{O}$ as a tropical rainfall indicator on G–I timescales (Fig. 1). Here, we use Mg/Ca (and Sr/Ca) in four southwest Sulawesi stalagmites spanning two G–I cycles to determine the suitability of $\delta^{18}\text{O}$ as a tropical rainfall indicator. We show that Sulawesi stalagmite Mg/Ca and Sr/Ca are primarily sourced from the limestone bedrock and subsequently altered by PCP. Variations in Mg/Ca and Sr/Ca of Sulawesi stalagmites with relatively slow growth are most likely driven by rainfall amount (i.e., PCP driven by infiltration, water residence time and void-space availability), whereas fast-growing stalagmites appear to be more strongly influenced by soil-karst processes (i.e., PCP driven by the influence of soil pCO₂ on upper void spaces and conduits exposed to root respiration). The coherent pattern of variability between the slow-growing Mg/Ca and all four Sulawesi speleothem $\delta^{18}\text{O}$ records makes it possible to robustly interpret changes in local rainfall through major climatic transitions. Our approach confirms a major increase in rainfall amount in the Australasian monsoon domain at glacial transitions that coincides with the largest shift in speleothem $\delta^{18}\text{O}$.

Study site and speleothem analysis. Stalagmites were collected from Abadi Cave in southwest Sulawesi, Indonesia (lat. 5.0°S, long. 119.7°E; elevation ~300 m above sea level). This region of southwest Sulawesi has highly seasonal rainfall, with the Indo-Australian summer monsoon delivering ~80% of annual rainfall between November and March. Mean annual temperature is 26.5 °C. High-elevation topography to the southeast of the study site, including Mount Lompobatang (elevation 2,874 m), prevents much of the austral winter monsoon rainfall (June–August), associated with southeast trade winds, from reaching the cave site¹².

Abadi Cave is ~320 m long and one of many systems carved within the Eocene to middle Miocene Tonasa Limestone Formation that covers much of the southwestern region of Sulawesi³⁹. The ground surface above the cave is characterised by karst and lowland intermediate forest with thin soil profiles⁴⁰. Abadi Cave has minor vertical changes of ±15 m and variable ceiling height. Although the cave's chambers are extensively decorated, active stalagmite growth has yet to be identified.

All stalagmite samples (Fig. 2) were collected ~250 m from the cave entrance. Stalagmites AC11-03 and AC11-02 grew in a large 'basement chamber' (~20 m across), while AC09-04 and AC11-06 were collected from a small 'side chamber' nearby and 10 m above the 'basement chamber'. Both chambers are isolated from the main entrance by a narrow crawl-through passageway. Stalagmite AC09-04 was found broken at the time of collection in 2009. The other three stalagmites were collected *in situ* in 2011 based on results from reconnaissance U-Th dating of mini-cores⁴¹ drilled in 2009. Limestone bedrock material was collected near the entrance of Abadi Cave in 2011 (Supplementary Methods).

Age models. The age-depth profiles of the Abadi Cave stalagmites are constrained by 34 high-precision U-Th dates ('Methods' and Supplementary Data 1 and online repository). Collectively, the geochemical records encompass ~100 ky of past climate, dating between 381 to 330 ky BP and 232 to 173 ky BP. Initial age-depth

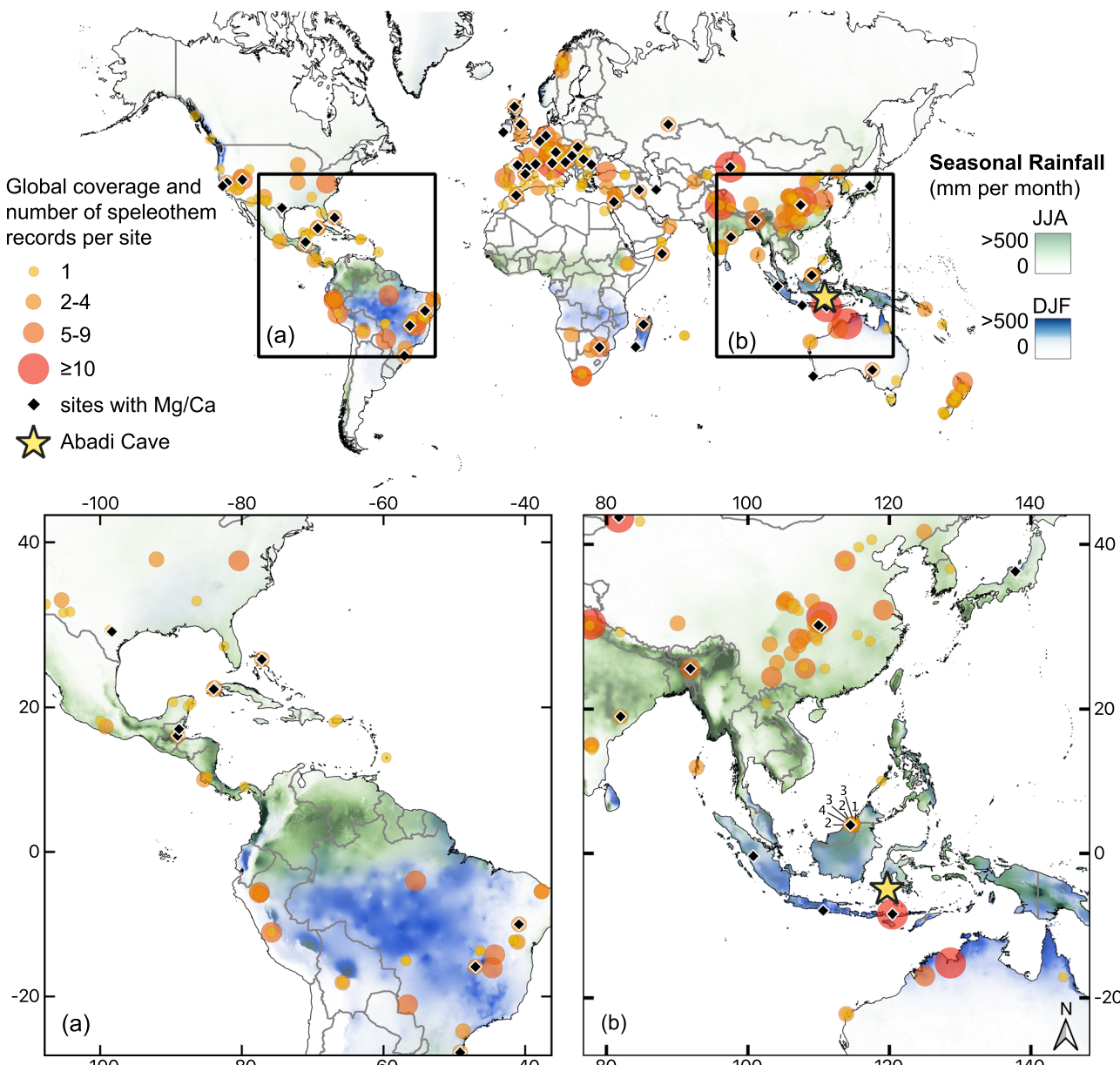


Fig. 1 Global distribution of speleothem $\delta^{18}\text{O}$ and Mg/Ca records and season-specific rainfall. The global map is accompanied by insets: **a** South American monsoon region and **b** Australasian monsoon region. These areas were selected to illustrate speleothem $\delta^{18}\text{O}$ record density and Mg/Ca presence. The yellow star marks the location of the Sulawesi speleothem $\delta^{18}\text{O}$ and Mg/Ca records for this study. Global speleothem locations are from the SISAL V2 database¹⁴. The number of speleothem entities associated with each site is indicated by colour and size of circles. Black dots denote sites with Mg/Ca data reported in SISAL V2. Because the northern Borneo sites are in close proximity to each other, resulting in overlapping dots, the number of stalagmite records is indicated with a line to each site (inset, **b**). In addition, a Mg/Ca marker was added over northern Borneo as the data exists⁸⁵ but is not recorded in the SISAL V2 database. Tropical rainfall for June–August (JJA, green scale) and December–February (blue scale) represents corresponding regional summer monsoon precipitation. Darker shades signify average monthly rainfall exceeding 500 mm. Precipitation data are from WorldClim 2.1 and span 1970–2000 at 5 min resolution⁸⁶. The map was created using QGIS software and country boundaries are based on the geometry from EBM v2020 scale 1:60 million (EuroGeographics and UNFAO⁸⁷).

models for each stalagmite were constructed with the U-Th dates and Bacon⁴², a Bayesian age-depth modelling tool implemented in geoChronR⁴³ to produce weighted mean age-depth models with 95% confidence intervals for each stalagmite (see 'Methods' and Supplementary Figs. S1 and S2).

The new stalagmite $\delta^{18}\text{O}$ timeseries for Sulawesi is well replicated, with common patterns clearly identified across sections of overlap (Fig. 3 and Supplementary Fig. S2). Therefore, the Bacon age models were optimised using linear interpolation between visual tie-points in the $\delta^{18}\text{O}$ records. Sections of the

Bacon age models were aligned by taking the average age of shared excursions and incorporating these sections into the original Bacon age-depth model. Importantly, all averaged tie-points and optimised age models fall within the age-depth uncertainties established using Bacon (Supplementary Fig. S2). Because the individual stalagmite $\delta^{18}\text{O}$, $\delta^{13}\text{C}$, Mg/Ca and Sr/Ca records are generated from the same sample aliquot, these age-depth models apply to each geochemical record described below. The age models show that growth rates for AC11-06 and AC09-04 (from the 'side chamber') are relatively slow (0.017 and



Fig. 2 Abadi Cave stalagmites analysed for this study. Photos of polished surfaces with sample milling tracks (black lines). U-Th date locations (black circles) are shown for each stalagmite. Note the uniform growth structure and clearly visible laminae on the slower-growing stalagmites, AC09-04 and AC11-06. The faster-growing stalagmites, AC11-02 and AC11-03, tend to be broader and less uniform (varying diameter), with subtle and intermittent laminae. AC11-03 contains growth unconformities (yellow bars); these segments are excluded from the analysis. Three U-Th dates associated with these unconformities (yellow circles) are excluded from the final age-depth model.

0.011 mm/y, respectively). In contrast, AC11-03 and AC11-02 (from the 'basement chamber') grew about four times faster (0.042 and 0.064 mm/y, respectively) with maximum growth occurring at deglacial transitions.

Coupled analysis of $\delta^{18}\text{O}$, $\delta^{13}\text{C}$, Mg/Ca and Sr/Ca. A total of 1253 stable-isotope measurements ($\delta^{18}\text{O}$ and $\delta^{13}\text{C}$) and 683 paired Mg/Ca and Sr/Ca measurements were made on aliquots of calcite powders micro-milled along the central growth axis of each stalagmite (see 'Methods'). Mg/Ca and Sr/Ca were measured via inductively coupled plasma atomic emission spectroscopy on every second sample for AC09-04 and AC11-06 and nearly every sample for AC11-02 and AC11-03.

Measurements of Mg/Ca and Sr/Ca were made on a sample of surface bedrock limestone to determine the relationship between bedrock and stalagmite values (see Supplementary Methods). Four spot-check analyses of Mg/Ca in the bedrock sample range from

12.1 to 13.2 mmol/mol, which is ~20 times higher than in the stalagmite samples. Bedrock Sr/Ca ranges from 0.24 to 0.28 mmol/mol, ~10 times higher than in the stalagmite samples. The large difference is due to the strong discrimination against Mg and Sr during the precipitation of stalagmite calcite from dripwaters³¹.

Results and discussion

Geochemical and growth-rate profiles for the four Sulawesi stalagmites are presented in Fig. 3. Stalagmite $\delta^{18}\text{O}$ values range between $-10.2\text{\textperthousand}$ and $-4.9\text{\textperthousand}$ after correction for the effect of ice volume^{44,45} (see Supplementary Methods). The effect of temperature change on speleothem $\delta^{18}\text{O}$ at our site is deemed to be negligible because the range of G-I change in $\delta^{18}\text{O}$ is much larger than can be explained by temperature¹². The older stalagmites, AC09-04 and AC11-02, have $\delta^{18}\text{O}$ values that are consistently $\sim 0.8\text{\textperthousand}$ lower than the younger stalagmites, AC11-06 and AC11-03. Stalagmite

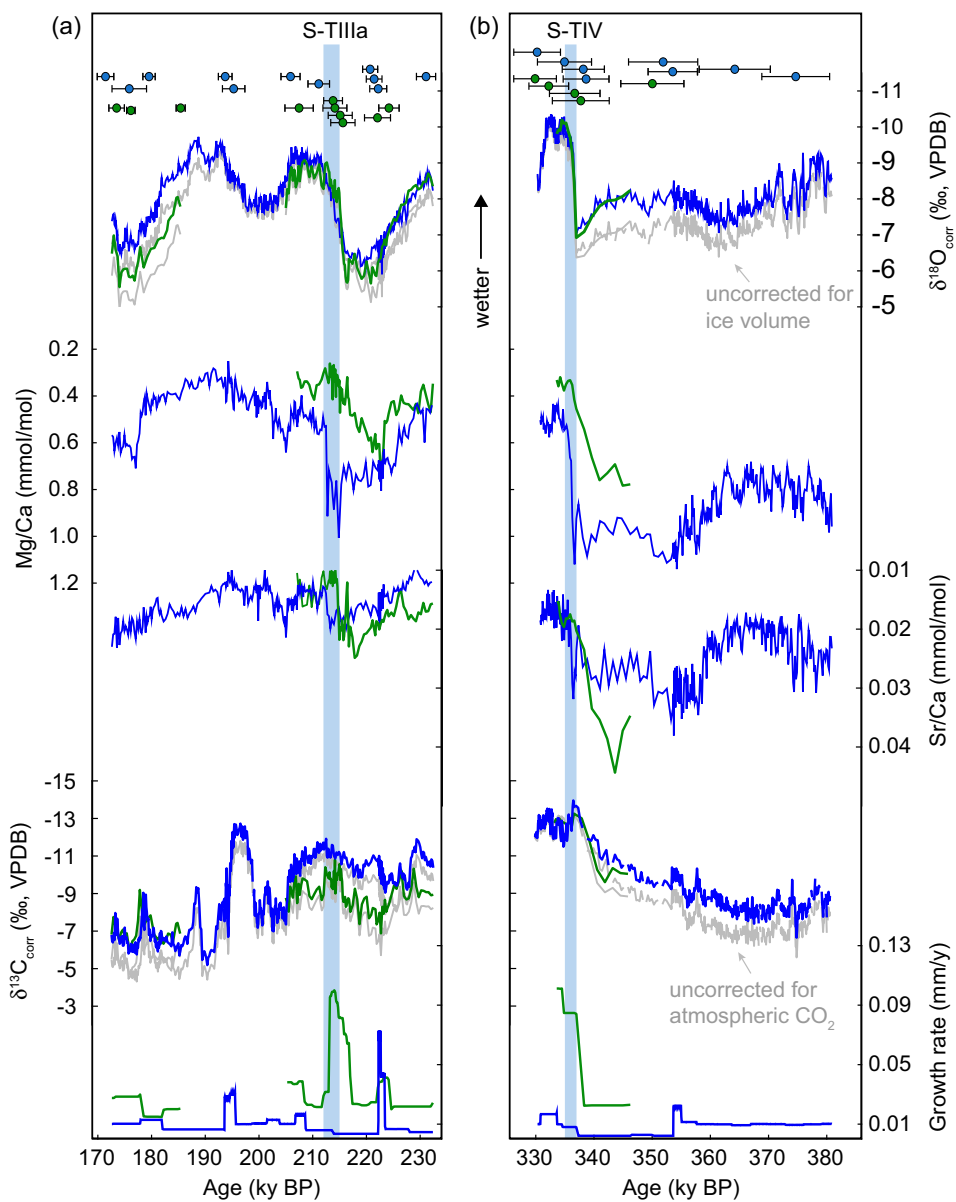


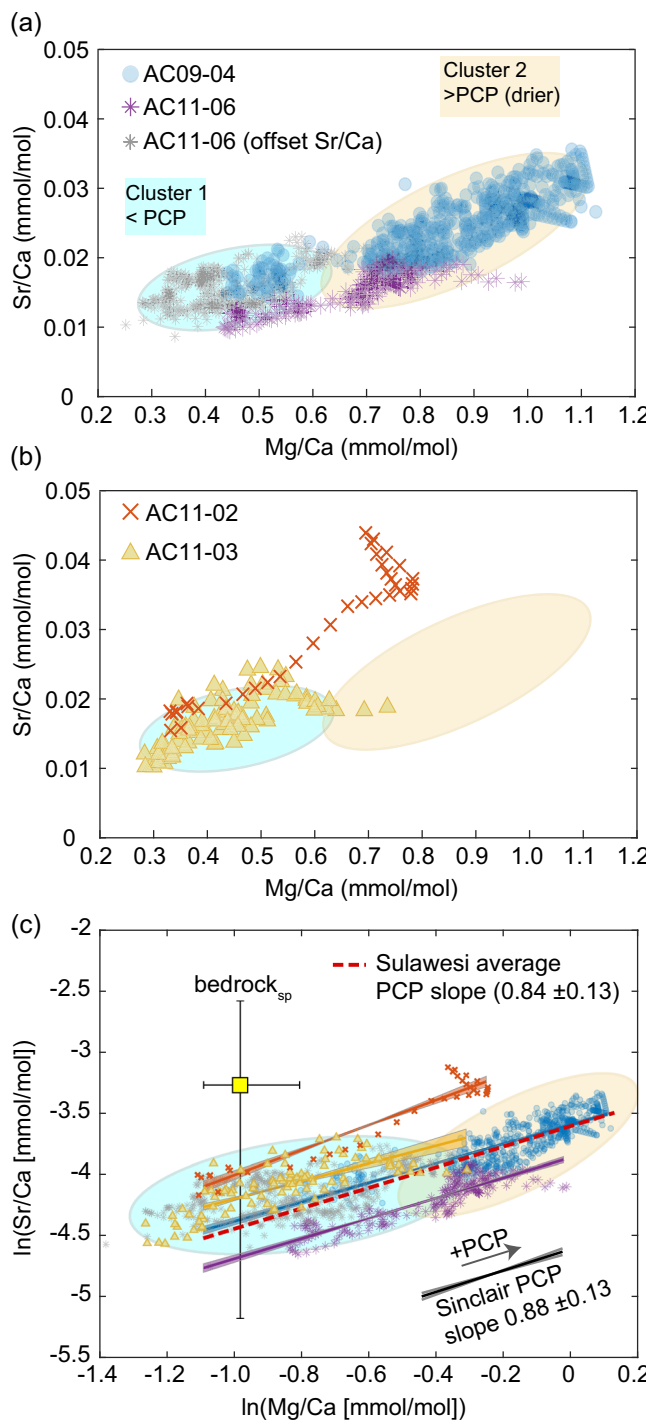
Fig. 3 Stalagmite $\delta^{18}\text{O}$, Mg/Ca, Sr/Ca, $\delta^{13}\text{C}$ and growth rates. a Stalagmites AC11-06 and AC11-03 spanning Sulawesi termination IIIa (S-TIIIa) and **b** AC09-04 and AC11-02 spanning Sulawesi termination IV (S-TIV). Geochemical data for fast-growing stalagmites (AC11-03, AC11-02) are shown in green, slow-growing stalagmites (AC11-06, AC09-04) are shown in blue. Stalagmite $\delta^{18}\text{O}$ has been corrected for the effect of ice volume⁴⁵ and stalagmite $\delta^{13}\text{C}$ has been corrected for the effect of atmospheric CO_2 ⁵³; the uncorrected records are shown in grey (see Supplementary Methods for details of these corrections). Sulawesi glacial terminations (determined by prominent shifts in Sulawesi stalagmite $\delta^{18}\text{O}$, Supplementary Methods) are indicated by blue bars. Colour-coded circles at the top of each panel show U-Th dates and their uncertainties (2σ). The y axes for geochemical profiles are inverted to show wetter conditions upward.

$\delta^{13}\text{C}$ values range between -14.0‰ and -5.2‰ after correction for atmospheric pCO_2 (see Supplementary Methods).

Mg/Ca and Sr/Ca for the younger stalagmites (AC11-06, AC11-03) range from 0.25 to 1.0 mmol/mol and 0.009 to 0.025 mmol/mol, respectively. The older stalagmites (AC09-04, AC11-02) have a slightly larger range of variability, with Mg/Ca values between 0.32 and 1.14 mmol/mol and Sr/Ca values between 0.013 and 0.044 mmol/mol. Due to the low concentrations of Sr in our samples, nearing instrumental detection limits, as well as limited consensus around Sr partition coefficients in the literature, we focus on Mg/Ca for comparative analyses with $\delta^{18}\text{O}$.

Karst recharge and PCP. Speleothem Mg, Sr and Ca are typically derived from the dissolved limestone bedrock and secondary

minerals along flow pathways, but can also be sourced from the soil and atmosphere^{26,32}. Bedrock dissolution, and associated incorporation of Mg, Sr and Ca into the seepage water, is driven by soil CO_2 and groundwater infiltration rates^{46,47}. Mg/Ca and Sr/Ca in speleothems are sensitive to changes in Ca from the feeding dripwaters through processes associated with soil and cave air CO_2 (soil-karst interactions) and water-rock interactions along flow pathways^{33,34,48}, referred to here as infiltration-PCP. If PCP occurs upstream of the cave drip site, the Mg/Ca and Sr/Ca will increase in the dripwater as Ca is preferentially lost from solution. Calcite precipitating from these waters on the speleothem surface will also be similarly co-enriched in Mg and Sr. PCP can occur when infiltration rates are low, drip intervals are long, or when cave CO_2 is low; these processes and combinations



of processes can differ depending on the individual dripwater flow pathways feeding a stalagmite^{30,46,49,50}.

Sulawesi stalagmite Mg/Ca and Sr/Ca positively and significantly co-vary ($r^2 = 0.57$, $P < 0.001$, $n = 651$) and demonstrate a constant slope when compared in cross-plot. These features indicate that PCP is a primary driver of Sulawesi stalagmite Mg/Ca and Sr/Ca variability^{27,34}. Using k-means cluster analysis, we identify two significant groupings of the Mg/Ca and Sr/Ca data for the Sulawesi stalagmites (Fig. 4). The Cluster 1 group has relatively low Mg/Ca and Sr/Ca values, supporting reduced PCP, while Cluster 2 has higher values, suggesting enhanced PCP. Cluster 1 mainly comprises the fast-growing stalagmite data and younger section of AC11-06 (212–173 ky BP), where Mg/Ca and

Fig. 4 Mg/Ca and Sr/Ca cluster analysis and ln-In PCP test. Elemental ratios for **a** slow-growing stalagmites and **b** fast-growing stalagmites. **c** Comparison of $\ln(\text{Mg/Ca})$ and $\ln(\text{Sr/Ca})$ with regressions and $\text{bedrock}_{\text{sp}}$ alongside the theoretical PCP slope of Sinclair et al.³⁴. The Sulawesi average PCP slope is calculated using the average of each stalagmite regression. Slopes shown for individual records were calculated from resampled data. Regressions on original (unevenly spaced) data made no significant difference in slopes (see Supplementary Fig. S3 and Supplementary Table S1). Data pairs in a section of AC11-06, with offset Sr/Ca (grey asterisks), show limited PCP and are not included in the average Sulawesi PCP regression. k-means cluster analysis of Mg/Ca and Sr/Ca for all Sulawesi stalagmites: Cluster 1 (blue ellipse, 1.5σ) grouping near average $\text{bedrock}_{\text{sp}}$ (yellow square with uncertainty range) is interpreted as minimal PCP while Cluster 2 (orange ellipse, 1.5σ) has evolved away from $\text{bedrock}_{\text{sp}}$ towards higher values, indicating enhanced PCP. Large uncertainties on $\text{bedrock}_{\text{sp}}$ correspond with the uncertainties in the Sinclair PCP slope equation used to determine the Sulawesi partition coefficient, K_{dSr} (Supplementary Methods). K-means cluster analysis (k-means clustering), ellipse determination (ELLIPSE) and linear regression (Linear Regression plot with Confidence Intervals) were performed and plotted in Matlab (<https://au.mathworks.com/matlabcentral/fileexchange/>).

Sr/Ca deviate from the rest of the stalagmite record (Fig. 4). This offset in AC11-06 may derive from wetter conditions that reduce the occurrence of PCP and potentially increase the chance of mixing water reservoirs with different trace element ratios (e.g., soil chemistry, re-routing of drip pathway). Thus, Mg/Ca is less effective as a hydroclimate indicator at times when the epikarst is nearing a saturated state^{26,31,32}.

Measured Mg/Ca and Sr/Ca values for Abadi Cave bedrock and estimated partition coefficients^{34,35,51} are used to calculate approximate Mg/Ca and Sr/Ca values for stalagmite calcite sourced entirely from the host rock, defined here as $\text{bedrock}_{\text{sp}}$ (see Supplementary Methods and Supplementary Fig. S3). Calculated $\text{bedrock}_{\text{sp}}$ values plot alongside stalagmite Mg/Ca and Sr/Ca ratios associated with Cluster 1 (Fig. 4). Proximity of Cluster 1 data to the calculated $\text{bedrock}_{\text{sp}}$ implies limited evolution away from the original bedrock composition and thus minimal PCP. Cluster 2 contains higher Mg/Ca and Sr/Ca values, which have evolved further away from the predicted $\text{bedrock}_{\text{sp}}$. These higher values indicate increased PCP, likely in response to reduced groundwater recharge and rainfall amount at the surface of the cave.

Given that Mg/Ca and Sr/Ca increase predictably as PCP proceeds^{27,31}, the ln-In relationship between Mg/Ca and Sr/Ca data can be used as an additional test for the occurrence of PCP (Fig. 4). Sinclair et al.³⁴ developed a mathematical model of PCP showing that $\ln(\text{Sr/Ca})$ versus $\ln(\text{Mg/Ca})$ produces a positive vector of constant slope that falls within a range of 0.75 to 1.01 (i.e., 0.88 ± 0.13). The average ln-In slope of Sulawesi Mg/Ca and Sr/Ca data is 0.84 ± 0.13 , which is within range of Sinclair's theoretical PCP slope and well within other reported ranges³⁵. Each Sulawesi stalagmite regression is slightly offset, indicating that the Mg and Sr content of individual stalagmites may be influenced by distinct dripwater flow pathways⁴⁶. The average ln-In regression of Sulawesi Mg/Ca and Sr/Ca was calculated using resampled data (determined by the median resolution of each record) to obtain evenly spaced increments. The average regression slope for the raw data is also within the resampled PCP range (Supplementary Table S1). The younger section of AC11-06 is excluded from these analyses due to the notable Sr/Ca offset occurring within the same stalagmite.

PCP determined by flow pathways. The two main drivers of PCP are (1) groundwater infiltration and availability of air-filled voids

within the karst aquifer (infiltration processes) and (2) pCO₂ content of air in the cave and void spaces (soil-karst processes)^{28,30,31,47}. Individual drip pathways and flow rates can determine which of these processes prevail for site-specific dripwaters^{46,48,49}. While rainfall amount and infiltration through the karst influence the extent of void space where PCP can occur, large G-I shifts in global temperature and CO₂ likely had a major effect on soil and cave air pCO₂ via vegetation productivity, microbial activity, and plant root respiration^{37,52,53}. Modern studies show that elevated mean annual temperature⁵⁴ and atmospheric CO₂ accelerate biogeochemical cycles and increase soil pCO₂^{55,56}.

Fracture and conduit flow pathways allow for seepage waters to be in contact with void air pCO₂ that may be more directly influenced by soil pCO₂^{31,57}. Here, the soil-influenced pCO₂ gradient between seepage water and the surrounding air of upper void spaces may drive PCP (Supplementary Fig. S4). For example, depending on the saturation state of seepage waters, void spaces with higher pCO₂ relative to seepage waters would prevent the occurrence of PCP, while void spaces with pCO₂ lower than seepage waters would increase PCP. In addition, because Ca prefers to be in a solid phase during dissolution and precipitation, corrosive seepage waters associated with higher soil pCO₂ may prompt greater dissolution of the bedrock and increase Ca ion release into solution^{30,57}—this process is linked to trace element partition coefficients and thus ratios evolve in a fashion that resembles PCP^{33,51}. Seepage waters flowing to stalagmites along a more direct fracture flow pathway would be more likely to retain this higher Ca (and thus lower trace element ratios), while longer diffuse flow pathways would provide greater opportunity for PCP (Ca loss), especially when infiltration rates are low.

Soil-karst PCP processes are likely to be recorded in Mg/Ca and Sr/Ca of stalagmites that formed from dripwaters with a more direct path from soil to stalagmite. Infiltration-driven PCP processes, resulting from residence time of seepage water and contact with cave and void-space air, are more likely to be imprinted in stalagmites fed by longer dripwater flow pathways. The δ¹³C signal from root respiration and vegetation productivity is likely to be retained in stalagmites regardless of the flow pathway, especially if this signal is much larger than the PCP influence on δ¹³C.

Optimal stalagmites for recording hydrology. Although both fast and slow-growing stalagmites have a PCP slope, Mg/Ca in fast-growing stalagmites remain relatively low, near bedrock_{sp} (Cluster 1), indicating limited PCP. The fast-growing specimens (~0.04–0.06 mm/y), are characterised by flat-topped growth laminations and relatively wide diameters that vary with height. In addition, both fast-growing specimens have ‘coffee-coloured’ calcite, indicative of organics and greater connectivity to the soil⁵⁸. Irregular features along the flanks of these stalagmites indicate high dripwater Ca concentration and high drip rates⁵⁸. Given the above, these stalagmites are likely fed by variable drip rates, with a combination of fracture flow and diffuse flow⁴⁸. Flow pathways for the fast-growing stalagmites may be subject to higher hydraulic loading, fewer air-filled voids and less water–rock interactions, resulting in a stronger chemical imprint from the soil and vadose zone.

The slow-growing stalagmites (AC09-04 and AC11-06) demonstrate a clear trend away from bedrock_{sp} towards more highly evolved Mg/Ca and Sr/Ca (spanning both Clusters 1 and 2). This suggests that PCP plays a larger role in their trace element chemistry than for fast growers. The slow-growing (~0.01–0.02 mm/y) Sulawesi stalagmites are uniformly narrow in diameter with conical growth laminae and likely fed by seepage

flow with relatively slow and regular drip intervals⁴⁸. Dripwaters feeding the slow-growing stalagmites are hypothesised to travel through longer flow pathways, with increased residence time and exposure to void space, leading to enhanced PCP during periods of low infiltration (Supplementary Fig. S4).

When the Mg/Ca and Sr/Ca timeseries are considered for slow and fast-growing stalagmites that grew over the same time period, there are distinct differences in trends, indicating that different processes are impacting site-specific flow pathways (Fig. 5). We note that the coeval stalagmite δ¹⁸O (and δ¹³C) records show excellent reproducibility and appear to be unaffected by differences in site-specific flow pathways. The slow-growing stalagmite Mg/Ca timeseries share the G-I baseline shift with stalagmite δ¹⁸O, transitioning to lower values near the end of glacial terminations. Conversely, Mg/Ca values in the faster-growing stalagmites are more coherent with stalagmite δ¹³C, atmospheric CO₂ fluctuations, and global temperature^{59–61}, where lower Mg/Ca and δ¹³C coincides with higher CO₂ and temperature (Fig. 5).

Given the faster growth rates and shared trends with temperature and atmospheric CO₂, we postulate that fast-growing stalagmite Mg/Ca was predominantly imprinted by large (G-I) changes in soil CO₂^{26,30,48}. The shared trends between fast-growing stalagmite Mg/Ca and coeval δ¹³C likely exist because both proxies are influenced directly or indirectly by soil pCO₂. Carbon in speleothem calcite is sourced primarily from soil CO₂ and bedrock carbonate⁶². Thus, speleothem δ¹³C (that has been corrected for the effect of atmospheric pCO₂ on ¹³C/¹²C fractionation in C₃ plants⁵³) can be interpreted to reflect variations in vegetation type, productivity, and root respiration above the cave^{37,53,62}. Although beyond the scope of this study, integrated modelling coupled with in-cave monitoring experiments would provide more insight into these soil-karst processes.

Because PCP associated with the slow-growing Sulawesi stalagmites is more likely to be influenced by rainfall amount and effective recharge, Mg/Ca in these stalagmites is better suited for hydrological reconstructions and comparison with δ¹⁸O. The exceptional length, reproducibility, and covariation of the slow-growing stalagmite records allow us to assess the validity of the heavily relied upon δ¹⁸O rainfall proxy across G-I transitions. We therefore focus on the slow-growing stalagmites for comparison of Mg/Ca and δ¹⁸O.

Coupled Mg/Ca- δ¹⁸O assessment of G-I transitions. The Mg/Ca values of the slow-growing stalagmites (AC11-06, AC09-04) share a prominent shift to lower values that coincides with the G-I transitions to lower δ¹⁸O. The good agreement between the paired proxies provides evidence for the preservation of a locally-relevant climatic signal⁶³. Additionally, the agreement between all four Sulawesi δ¹⁸O records and PCP-sensitive Mg/Ca of the slow-growing stalagmites indicates that both proxies are responding to rainfall amount at the Sulawesi glacial termination²⁶. The onset of major G-I shifts in Sulawesi δ¹⁸O and Mg/Ca are identified using Bayesian change-point analysis⁶⁴ (Supplementary Fig. S5). Stalagmite δ¹⁸O undergoes a 3‰ shift to lower values over a 2–3 ky period, from ~337 to 335 ky BP and ~215 to 212 ky BP. These shifts occur in the later stages of global deglaciation, after weak monsoon intervals (WMIs) identified in China^{5,6}, and are referred to here as Sulawesi glacial terminations: S-TIV and S-TIIIa. The Mg/Ca in the slow-growing stalagmites also undergoes a baseline shift to lower values during the δ¹⁸O transitions. The response of Mg/Ca, as δ¹⁸O begins to decrease, is characterised initially by brief pulse(s) to higher values, followed by a rapid transition to low interglacial values, coinciding with the completion of the δ¹⁸O shift. The common trend of the two proxy

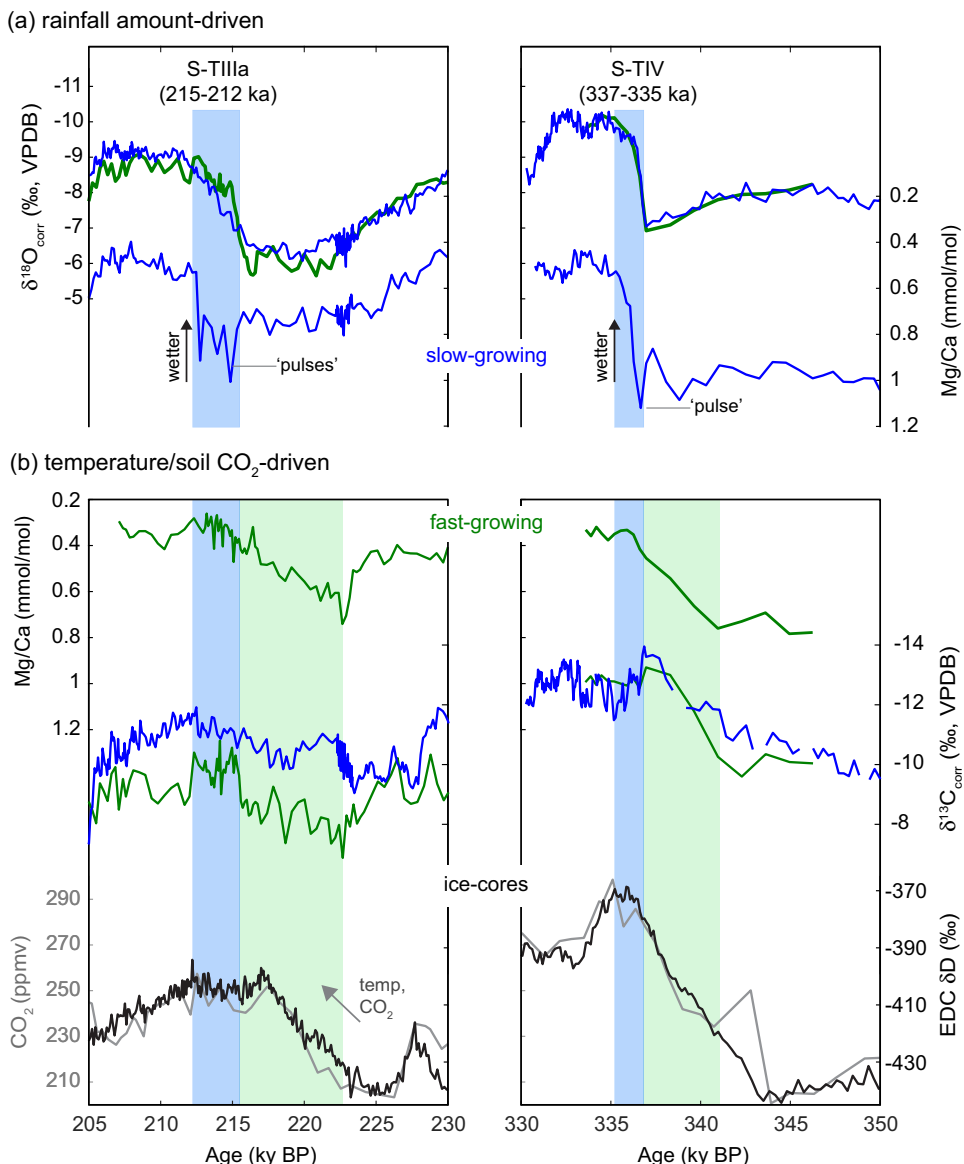


Fig. 5 Sulawesi stalagmite proxies driven by rainfall amount versus temperature and soil CO_2 . **a** Sulawesi stalagmite $\delta^{18}\text{O}$ records (corrected for ice volume) and slow-growing stalagmite Mg/Ca and all stalagmite $\delta^{13}\text{C}$ records compared with Vostok ice core measurements of atmospheric CO_2 (grey) and EPICA Dome C deuterium (black) plotted on the AICC chronology^{59–61} (lower panel). The gradual trend in the fast-growing stalagmite Mg/Ca (green) corresponds with changes in stalagmite $\delta^{13}\text{C}$ (corrected for atmospheric CO_2 effect), atmospheric CO_2 and global temperature/δD (grey arrows). This Mg/Ca response is attributed to soil-karst processes, driven by vegetation changes (green bars). The step-change in the slow-growing stalagmite Mg/Ca (blue) corresponds with the deglacial transition in $\delta^{18}\text{O}$ and is attributed to water-karst PCP processes driven by infiltration. Note the pulses during Sulawesi glacial terminations S-TIIa (215–212 ky BP) and S-TIV (337–335 ky BP), interpreted as a response to increased infiltration (see text for details). The durations of S-TIIa (215–212 ky BP) and S-TIV (337–335 ky BP) are based on all four stalagmite $\delta^{18}\text{O}$ change points and coinciding change points in slow-growing stalagmite Mg/Ca (blue bars, Supplementary Fig. S5).

datasets is consistent with drier glacial conditions with enhanced PCP, followed by increased rainfall and reduced/absent PCP during interglacials.

There is an obvious lag between the Mg/Ca and $\delta^{18}\text{O}$ transitions over the Sulawesi glacial terminations recorded by the slow-growing stalagmites. Using cross-correlation analysis, we find that the correlation between the two proxies, across the deglacial transitions, is optimised when Mg/Ca is shifted to older by a few hundred years. The Mg/Ca glacial transition lags $\delta^{18}\text{O}$ by approximately ~200–300 years across S-TIV (342–332 ky BP) and ~500–700 years across S-TIIa (220–210 ky BP) (see Supplementary Fig. S6). Because the Mg/Ca and $\delta^{18}\text{O}$ measurements were

made on the same sample aliquots, the lag cannot be due to chronological offsets between the two records. The most likely explanation for a lag between the two proxies is that it takes longer to fill voids and saturate diffuse flow pathways (indicated by Mg/Ca) than for seepage water to reach the stalagmite surface itself (indicated by $\delta^{18}\text{O}$)^{26,65}. For example, if a relatively dry karst network experiences a dramatic increase in recharge due to increased rainfall, back-filling and saturation of the epikarst may take hundreds of years to measurably suppress the PCP system and dripwater Mg/Ca, whereas dripwater $\delta^{18}\text{O}$ would be influenced quickly by a change in the $\delta^{18}\text{O}$ of rainwater. When the karst network finally recovers from an extended glacial period

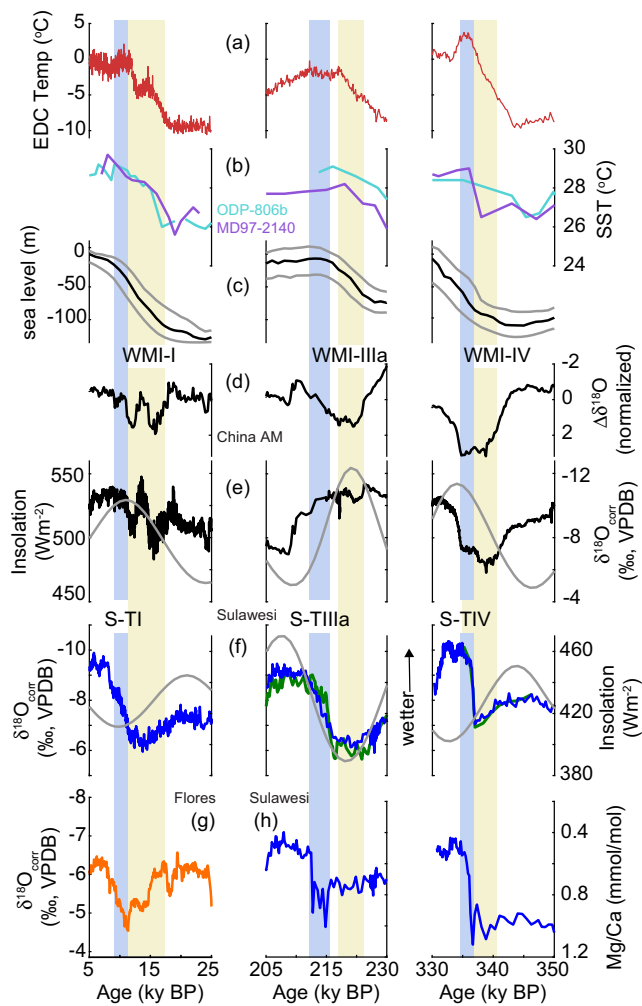


Fig. 6 Comparison between Australasian monsoon and glacial-interglacial climate transitions. **a** EPICA Dome C (EDC) estimated temperature difference (relative to the last 1000 years)^{60,61}. **b** Sea surface temperature (SST) from the Ontong Java Plateau (ODP 806B, cyan)⁸⁸ and West Pacific Warm Pool (MD97-2140, purple)⁸⁹. **c** Global sea level stack⁹⁰. **d** Suborbital Asian Monsoon (AM) component ($\Delta\delta^{18}\text{O}$, detrended from the composite stalagmite $\delta^{18}\text{O}$ record from China by subtracting summer insolation)⁶ showing weak monsoon intervals (WMIs, yellow bars). **e** Composite speleothem $\delta^{18}\text{O}$ records from China^{5,91-93} and 21 June insolation at 65°N⁹⁴. **f** Speleothem $\delta^{18}\text{O}$ records from Sulawesi: S-TIV, S-TIIa (this study) and S-TI¹² and 21 January insolation at 5°N⁹⁴. **g** Composite speleothem $\delta^{18}\text{O}$ record from Flores^{11,13}. **h** Mg/Ca records from slow-growing Sulawesi stalagmites (this study). S-TIIa and S-TIV (blue bars), are based on all four Sulawesi stalagmite $\delta^{18}\text{O}$ change points and coinciding change points in slow-growing stalagmite Mg/Ca.

of low infiltration, the replenished water moving through the system is likely to entrain trace metals that have built up along flow pathways during the dry periods and deposit them onto stalagmite surfaces²⁶. In addition, cation exchange (Na for Mg) and the release of Mg from soils above the cave has been observed when rainfall increases following a prolonged dry period⁶⁶. Thus, the brief pulse(s) towards higher Mg/Ca values occurring over both Sulawesi terminations may signal the initial back-filling of the epikarst and/or cation exchange from soils. The final Mg/Ca shift to interglacial values at each termination coincides with the conclusion of the $\delta^{18}\text{O}$ transition, however, the Mg/Ca pulses over S-TIIa are more apparent and occur over a longer period of time (~2.5 ka) compared to S-TIV. This extended delay, prior to

Mg/Ca achieving interglacial values, could be due to the amount and regularity of increased rainfall over the transition at S-TIIa or a more extensive flow pathway network feeding the stalagmite.

Sulawesi terminations and global implications. Changes in deep atmospheric convection over the maritime continent are hypothesised to dominate hydroclimate over the last glacial period, resulting in reduced convection associated with the Australasian monsoon during the last glacial, followed by rapid monsoon strengthening in the final stages of deglaciation¹². The Sulawesi paired stalagmite $\delta^{18}\text{O}$ and Mg/Ca records spanning TIV and TIIa, combined with the last glacial Sulawesi stalagmite $\delta^{18}\text{O}$ record¹², provide strong evidence for reduced rainfall and a weakened Australasian summer monsoon spanning glacial maxima, deglacial onset, and WMIs in China^{5,6}. These prolonged periods of reduced rainfall in the northern (e.g., WMIs) and southern hemisphere sectors of the Australasian monsoon also correspond with glacial drying in northern Borneo^{7,8,10}. These periods of reduced rainfall occur despite rising global temperatures and warm pool sea surface temperatures and under various phases of insolation forcing (Fig. 6 and Supplementary Fig. S7). Previous work has proposed a southward shift in the Australasian monsoon rainbelt and ITCZ during cold intervals in the northern hemisphere and glacial terminations^{5-8,10-13,67}. This southward shift is attributed to the collapse of the northern hemisphere ice sheets, associated slow-down of Atlantic meridional overturning circulation, increased interhemispheric temperature gradients, and a poleward shift of the austral westerlies. Together, these events prompt CO_2 upwelling from the Southern Ocean and enhanced heat transport across the planet⁶⁸⁻⁷¹.

Reduced rainfall in Sulawesi throughout WMIs is surprising since the study site is located 5°S of the equator, where an increase in rainfall might be expected as the Australasian monsoon shifts southward. Instead, it appears that the tropical rainbelt and associated summer monsoon was likely shifted further south beyond Sulawesi and/or convection was greatly reduced over the IPWP. Sea level-driven changes in landmass configuration of the maritime continent are thought to contribute to a reduction in IPWP convection (drying) during the glacial maxima⁷²⁻⁷⁴, thus it is possible that both a southward shift in the rainbelt and reduced convection influenced Sulawesi rainfall. A southward shift of the tropical rainbelt in response to interhemispheric temperature gradients at the onset of WMIs in China^{5,6} is supported by stalagmite records spanning the IPWP and Australasian monsoon region, where wetter conditions develop in Flores^{11,13} and northern Australia⁶⁷ and drying occurs in Borneo^{7,8,10} and Sulawesi (this study and ref. ¹²). Model and proxy results indicate that a southward shift of an anomalous anticyclone during the austral summer, as a result of the slow-down of the Atlantic meridional overturning circulation, resulted in drying over the IPWP maritime continent during Heinrich Stadial 1 (at the onset of WMI-I)⁷⁵. The increase in Sulawesi rainfall and return of IPWP hydroclimate to interglacial conditions coincides with rising sea levels, likely as a result of increased convection as the maritime continent floods^{72,73}. The establishment of interglacial conditions in the Australian summer monsoon also coincides with the stabilisation of interglacial SSTs and global temperature, therefore a sea level and/or temperature threshold may be required to trigger reinvigoration of IPWP convection and associated rainfall.

The Sulawesi stalagmite $\delta^{13}\text{C}$ and fast-growing stalagmite Mg/Ca support an increase in vegetation productivity at the onset of global deglaciation and WMIs that corresponds with changes in temperature and atmospheric CO_2 . This transition occurs ~4–7 ky earlier than Sulawesi rainfall intensification. Similar

disconnects between rainfall amount and vegetation change were identified in New Zealand over the Last Glacial Maximum, where multi-proxy stalagmite data support an increase in rainfall above the cave occurring 2 ky after a substantial post-glacial increase in forest extent⁶⁵. A stalagmite record from northern Borneo also shows evidence for decoupling between G-I temperature and hydroclimate over the last glacial termination, where cave temperatures track changes in ice core CO₂, corresponding to Antarctic warming, whereas regional hydroclimate responds more strongly to millennial-scale northern hemisphere cooling events⁷⁶. A disconnect between tropical temperature and hydroclimate across G-I transitions highlights the importance of distinguishing the prevailing climatic driver when interpreting paleoclimate proxies from these regions.

There is a notable mismatch in the Sulawesi stalagmite Mg/Ca and δ¹⁸O from 375–355 ky BP when PCP is present (Supplementary Fig. S8). The mismatch in the coupled record may indicate changes in the seasonal balance of rainfall, where variations in δ¹⁸O are driven by changes in rainfall source and trajectories, rather than rainfall amount^{77,78}. Seasonal changes in the position of the ITCZ and Australasian monsoon moisture-transport pathways are accompanied by large latitudinal gradients in the δ¹⁸O of rainfall^{16,22}. The unexpectedly high rainfall δ¹⁸O in Sulawesi around 375–355 ky BP corresponds to lower amplitude changes in summer insolation and relatively high monsoon rainfall in China⁵. Thus, a northward bias in the position of the ITCZ or reduced seasonality (a change in the dominant source of Sulawesi rainfall) could decrease the contribution of isotopically light austral summer rainfall and tip the oxygen-isotope water balance in southwest Sulawesi toward isotopically heavier austral winter rainfall. In addition, variability in the Pacific Walker Circulation could influence regional rainfall δ¹⁸O through changes in zonal moisture-transport pathways and rainfall amount⁷⁸. Therefore, unexpectedly high rainfall δ¹⁸O in Sulawesi over this period could also be attributed to a weaker or displaced Pacific Walker Circulation that does not necessarily reflect changes in local rainfall amount^{10,17}.

Conclusions. The results presented here demonstrate the potential for multi-proxy records of stalagmite δ¹⁸O, Mg/Ca, Sr/Ca and δ¹³C to provide tighter constraints on interpretations of hydroclimate variation in the deep tropics, where records of δ¹⁸O alone can be ambiguous. A key finding from the coupled Mg/Ca and δ¹⁸O records for Sulawesi is that glacial cycles in the core of the Australasian monsoon domain are characterised by a prominent and relatively rapid shift from dry glacials, coinciding with WMIs in China, to wet interglacials during the final stages of global deglaciation. This increase in Sulawesi rainfall is decoupled from global temperature and tropical SSTs and occurs ~4–7 ky after temperatures begin to rise. Differences between Mg/Ca and δ¹⁸O in sections of the record where PCP is evident indicate that Sulawesi δ¹⁸O may not always strictly record rainfall amount. At these times, rainfall δ¹⁸O likely retains a combined signal of rainfall amount and the source or regional system from which that rain formed. With further development, discrepancies in coupled records of Mg/Ca and δ¹⁸O for near-equatorial settings could become a powerful tool for distinguishing the relative contributions of summer and winter rainfall (with contrasting δ¹⁸O) to the monsoon water balance.

An important goal for the paleoclimate community will be to establish criteria for identifying cave sites containing speleothems with PCP signals driven by groundwater infiltration. Our results indicate that slow-growing and uniform stalagmites, located in sections of the cave with diffuse flow, are the most likely candidates to contain PCP signals indicative of rainfall amount.

Our results highlight that soil processes influencing pCO₂ of void space can drive Mg/Ca variability in fracture-fed stalagmites, thus recording climatic changes that are unrelated to infiltration-driven PCP. Stalagmite δ¹³C, responding to vegetation productivity and root respiration above the cave, may co-vary with Mg/Ca that has also been influenced by soil-related processes. An international effort to perform trace element analysis on existing high-quality, well-dated and relatively slow-growing stalagmites that have corresponding δ¹⁸O measurements could provide a wealth of knowledge on tropical climate dynamics.

Methods

Sample preparation. Following collection, stalagmites were cut in half and slabbed at ~15-mm thickness along the central plane of growth. Our method for sequential extraction of carbonate micro-samples from the specimens was adapted from existing techniques^{32,79}. Briefly, calcite powders for stable isotopes (δ¹⁸O, δ¹³C) and minor elements (Mg/Ca, Sr/Ca) were milled from the central growth axis of each stalagmite using a Sheridan GCM Micromill. A 1-mm-diameter end-mill bit was used to collect high-resolution samples and a 2-mm-diameter end-mill bit for low-resolution samples. High-resolution samples were milled continuously from stalagmites AC09-04 and AC11-06 at 0.8 mm and 1.2 mm increments, resulting in sample resolutions of 90–130 years and 40–180 years, respectively. The low-resolution samples were milled at 10 and 30 mm increments, yielding a sample resolution ranging between 80–740 years for AC11-03 and 460–1890 years for AC11-02. High-resolution sampling was not performed on AC11-03 and AC11-02, as these samples were primarily intended for replication and high resolution was not necessary. Four spot samples were milled for Mg/Ca and Sr/Ca analysis from clean, pre-milled surfaces of a single piece of surface limestone bedrock material.

Uranium-thorium dating. Material for uranium-thorium (U-Th) dating was extracted from pre-cleaned surfaces of slabbed stalagmites using an impulse high torque air-drill fitted with a miniature circular saw blade. The saw blade was continuously lubricated with demineralised water while cutting. For each date, four cuts were made into the material allowing for the extraction of a solid block weighing 130–200 mg. Numerous reconnaissance U-Th dates for this work were measured at the National Taiwan University's High-Precision Mass Spectrometry and Environment Change Laboratory (HISPEC). The majority of the 34 dates for the age models used in this study were performed at the University of Minnesota Trace Metal Isotope Geochemistry Group (TMIG). The methodology for measuring U and Th isotopes by multi-collector inductively coupled plasma mass spectrometry (MC-ICP-MS) is described in refs. ^{80,81} and ref. ⁸². All U-Th isotope results and age determinations can be found in Supplementary Data 1 and in the online repository. U-Th dates, relative to CE 1950, were corrected using the initial ²³⁰Th value that minimised age reversals (Supplementary Fig. S1). Age errors (2σ) on U-Th dates range from 0.5 to 1.8%.

Age models. We used Bacon software⁴², implemented through geoChronR⁴³, to construct initial age models for the stalagmite records in this study (Supplementary Figs. S1 and S2). Bacon is an age-depth modelling approach that uses Bayesian statistics to reconstruct accumulation histories based on U-Th dates and uncertainties. Millions of Markov Chain Monte Carlo (MCMC) iterations are used to estimate accumulation rates between depths, using information provided by U-Th dates and input parameters, such as estimated mean accumulation rates, memory, and sample thickness/slices. Bacon output consists of a weighted mean age-depth model with 95% confidence intervals. The Bacon age models were then optimised using linear interpolation between visual tie-points in the δ¹⁸O records (Supplementary Figs. S1 and S2). The tie-points and optimised age models for each stalagmite fall within the 95% confidence intervals of the original Bacon age-depth models.

Stable-isotope analysis. Measurements of stalagmite δ¹⁸O and δ¹³C were made at the Australian National University (ANU) using Finnigan MAT-251 and Thermo MAT-253 mass spectrometers, each coupled to a Kiel microcarbonate preparation device. To ensure consistency among runs, in-run measurements of the NBS-19 standard (δ¹⁸O = -2.20‰; δ¹³C = -1.95‰) were made for every 5–8 samples, complemented by less frequent measurements of NBS-18 (δ¹⁸O = -23.0‰; δ¹³C = -5.0‰). Results are reported relative to Vienna PeeDee Belemnite (VPDB). The in-run analytical error for NBS-19, averaged for each run, is ±0.05‰ for δ¹⁸O and ±0.02‰ for δ¹³C (*n* = 375, 1σ). The mean standard error for duplicate analyses on sample aliquots was ±0.03‰ for δ¹⁸O and ±0.01‰ for δ¹³C (*n* = 64). Quantifying sample measurement reproducibility demonstrates that variability down to around 0.1‰ in the stalagmite δ¹⁸O and δ¹³C profiles is not due to measurement uncertainty. The powder samples for AC09-04 were alternately measured between instruments (i.e., odd-numbered samples on the MAT-253, even-numbered samples on the MAT-251). No significant offsets for δ¹⁸O and δ¹³C measurements were detected between the instruments for the purposes of this study.

Minor element measurements. Measurements of Mg/Ca and Sr/Ca in stalagmite samples were measured on the same sample powders used for the stable-isotope analyses using Varian Vista AX inductively coupled plasma atomic emission spectroscopy (ICP-AES) at the ANU. For the stalagmites milled at high resolution, every other sample was measured on the ICP-AES to preserve half of the sample material for future analyses. The ICP-AES analysis was based on methods described in Schrag (ref. ⁸³) where a ~1 mg aliquot of carbonate powder was dissolved in 5 mL of 2% HNO₃. Each sample solution underwent ten replicate analyses, with the final mmol/mol ratio reported as the average of all ten replicate ratios. The internal precision of replicate measurements averaged over all runs is $\pm 1.0\%$ for Mg/Ca (mmol/mol) and $\pm 1.7\%$ for Sr/Ca (mmol/mol).

To standardise the ICP-AES data and account for potential instrument drift, standard-sample-standard bracketing was employed. ANU coral bracketing standards (Mg/Ca = 5.754 mmol/mol, Sr/Ca = 8.983 mmol/mol) were prepared from high purity CaCO₃, SrCO₃, and an AccuTrace 1000 ppm Mg standard, dissolved in 2% HNO₃. Bracketing standard trace element ratios were previously validated by thermal ionisation mass spectrometry (TIMS) against an accepted ANU in-house standard. Bracketing standards had an average in-run precision of $\pm 0.45\%$ for Mg/Ca and $\pm 0.29\%$ for Sr/Ca (RSD, average of 64 analyses per run) over the course of 5–10 h runs. Because the coral bracketing standard has higher concentrations of Sr than the Sulawesi stalagmite calcite, instrument rinse times between samples were increased to 180 s to avoid memory effects.

An additional synthetic standard with low Sr concentrations similar to those observed for southwest Sulawesi stalagmites (Sr/Ca = 0.02 mmol/mol), was used to test instrument detection limits. The precision for Sr/Ca ratios from the low Sr standard measurements was $\pm 0.43\%$ ($n = 20$, 1 RSD), thus demonstrating that the instrument is capable of precisely measuring low Sr concentrations. In-run measurements of the JCp-1 standard were also made to check the reproducibility among runs. Measurements for Mg/Ca and Sr/Ca ratios of JCp-1 (Mg/Ca = 4.125 ± 0.028 , Sr/Ca = 8.766 ± 0.032 , $n = 11$) are within error of those reported in ref. ⁸⁴ (Mg/Ca = 4.199 ± 0.065 , Sr/Ca = 8.838 ± 0.089), with a measurement precision of $\pm 0.25\%$ ($n = 11$, 1 RSD).

Data availability

Geochemical data and stalagmite chronologies that support the findings of this study can be found on the NOAA Paleoclimatology Data online repository at <https://www.nci.noaa.gov/access/paleo-search/study/38025>. U-Th dating results are provided as Supplementary Data 1 and online.

Received: 22 June 2022; Accepted: 30 May 2023;

Published online: 13 June 2023

References

- Haywood, A. M. et al. What can palaeoclimate modelling do for you? *Earth Syst. Environ.* **3**, 1–18 (2019).
- Muthayya, S., Sugimoto, J. D., Montgomery, S. & Maberly, G. F. An overview of global rice production, supply, trade, and consumption. *Ann. N. Y. Acad. Sci.* **1324**, 7–14 (2014).
- Gaupp, F., Hall, J., Hochrainer-Stigler, S. & Dadson, S. Changing risks of simultaneous global breadbasket failure. *Nat. Clim. Chang.* **10**, 54–57 (2020).
- Cruz, F. W. Jr. et al. Evidence of rainfall variations in Southern Brazil from trace element ratios (Mg/Ca and Sr/Ca) in a Late Pleistocene stalagmite. *Geochim. Cosmochim. Acta* **71**, 2250–2263 (2007).
- Cheng, H. et al. Ice age terminations. *Science* **326**, 248–252 (2009).
- Cheng, H. et al. The Asian monsoon over the past 640,000 years and ice age terminations. *Nature* **534**, 640–646 (2016).
- Partin, J. W., Cobb, K. M., Adkins, J. F., Clark, B. & Fernandez, D. P. Millennial-scale trends in west Pacific warm pool hydrology since the Last Glacial Maximum. *Nature* **449**, 452–455 (2007).
- Meckler, A. N., Clarkson, M. O., Cobb, K. M., Sodemann, H. & Adkins, J. F. Interglacial hydroclimate in the tropical west Pacific through the Late Pleistocene. *Science* **336**, 1301–1304 (2012).
- Carolin, S. A. et al. Varied response of western Pacific hydrology to climate forcings over the last glacial period. *Science* **340**, 1564–1566 (2013).
- Carolin, S. A. et al. Northern Borneo stalagmite records reveal West Pacific hydroclimate across MIS 5 and 6. *Earth Planet. Sci. Lett.* **439**, 182–193 (2016).
- Ayliffe, L. K. et al. Rapid interhemispheric climate links via the Australasian monsoon during the last deglaciation. *Nat. Commun.* **4**, 1–6 (2013).
- Krause, C. E. et al. Spatio-temporal evolution of Australasian monsoon hydroclimate over the last 40,000 years. *Earth Planet. Sci. Lett.* **513**, 103–112 (2019).
- Scroxton, N. et al. Antiphase response of the Indonesian–Australian monsoon to millennial-scale events of the last glacial period. *Sci. Rep.* **12**, 1–12 (2022).
- Comas-Bru, L. et al. SISALv2: a comprehensive speleothem isotope database with multiple age-depth models. *Earth Syst. Sci. Data Discuss.* 1–47 <https://doi.org/10.5194/essd-2020-39> (2020).
- Lewis, S. C. et al. High-resolution stalagmite reconstructions of Australian–Indonesian monsoon rainfall variability during Heinrich stadial 3 and Greenland interstadial 4. *Earth Planet. Sci. Lett.* **303**, 133–142 (2011).
- Griffiths, M. L. et al. Increasing Australian–Indonesian monsoon rainfall linked to early Holocene sea-level rise. *Nat. Geosci.* **2**, 636–639 (2009).
- Moerman, J. W. et al. Diurnal to interannual rainfall $\delta^{18}\text{O}$ variations in northern Borneo driven by regional hydrology. *Earth Planet. Sci. Lett.* **369–370**, 108–119 (2013).
- Caley, T., Roche, D. M. & Renssen, H. Orbital Asian summer monsoon dynamics revealed using an isotope-enabled global climate model. *Nat. Commun.* **5**, 1–6 (2014).
- Konecky, B., Russell, J. & Bijaksana, S. Glacial aridity in central Indonesia coeval with intensified monsoon circulation. *Earth Planet. Sci. Lett.* **437**, 15–24 (2016).
- Liu, G. et al. On the glacial–interglacial variability of the Asian monsoon in speleothem $\delta^{18}\text{O}$ records. *Sci. Adv.* **6**, 1–11 (2020).
- Nilsson-Kerr, K., Anand, P., Holden, P. B., Clemens, S. C. & Leng, M. J. Dipole patterns in tropical precipitation were pervasive across landmasses throughout Marine Isotope Stage 5. *Commun. Earth Environ.* **2**, 1–9 (2021).
- Cobb, K. M., Adkins, J. F., Partin, J. W. & Clark, B. Regional-scale climate influences on temporal variations of rainwater and cave dripwater oxygen isotopes in northern Borneo. *Earth Planet. Sci. Lett.* **263**, 207–220 (2007).
- Griffiths, M. L. et al. Western Pacific hydroclimate linked to global climate variability over the past two millennia. *Nat. Commun.* **7**, 1–9 (2016).
- Magiera, M. et al. Local and regional Indian Summer Monsoon precipitation dynamics during Termination II and the Last Interglacial. *Geophys. Res. Lett.* **46**, 12454–12463 (2019).
- Liu, Y. H. et al. Links between the East Asian monsoon and North Atlantic climate during the 8,200 year event. *Nat. Geosci.* **6**, 117–120 (2013).
- Fairchild, I. J. & Treble, P. C. Trace elements in speleothems as recorders of environmental change. *Quat. Sci. Rev.* **28**, 449–468 (2009).
- Tremaine, D. M. & Froelich, P. N. Speleothem trace element signatures: a hydrologic geochemical study of modern cave dripwaters and farmed calcite. *Geochim. Cosmochim. Acta* **121**, 522–545 (2013).
- Spötl, C., Fairchild, I. J. & Tooth, A. F. Cave air control on dripwater geochemistry, Obir Caves (Austria): Implications for speleothem deposition in dynamically ventilated caves. *Geochim. Cosmochim. Acta* **69**, 2451–2468 (2005).
- Baker, A., Flemons, I., Andersen, M. S., Coleborn, K. & Treble, P. C. What determines the calcium concentration of speleothem-forming drip waters? *Glob. Planet. Change* **143**, 152–161 (2016).
- Stoll, H. M., Müller, W. & Prieto, M. I-STAL, a model for interpretation of Mg/Ca, Sr/Ca and Ba/Ca variations in speleothems and its forward and inverse application on seasonal to millennial scales. *Geochem. Geophys. Geosyst.* **13**, 1–27 (2012).
- Fairchild, I. J. et al. Controls on trace element (Sr–Mg) compositions of carbonate cave waters: implications for speleothem climatic records. *Chem. Geol.* **166**, 255–269 (2000).
- Fairchild, I. J. et al. Modification and preservation of environmental signals in speleothems. *Earth-Science Rev.* **75**, 105–153 (2006).
- Sinclair, D. J. Two mathematical models of Mg and Sr partitioning into solution during incongruent calcite dissolution. *Chem. Geol.* **283**, 119–133 (2011).
- Sinclair, D. J. et al. Magnesium and strontium systematics in tropical speleothems from the Western Pacific. *Chem. Geol.* **294**, 1–17 (2012).
- Wassenburg, J. A. et al. Calcite Mg and Sr partition coefficients in cave environments: Implications for interpreting prior calcite precipitation in speleothems. *Geochim. Cosmochim. Acta* **269**, 581–596 (2020).
- Wong, C. I. & Brecker, D. O. Advancements in the use of speleothems as climate archives. *Quat. Sci. Rev.* **127**, 1–18 (2015).
- Fohlmeister, J. et al. Main controls on the stable carbon isotope composition of speleothems. *Geochim. Cosmochim. Acta* **279**, 67–87 (2020).
- Cheng, H. et al. Climate variations of Central Asia on orbital to millennial timescales. *Sci. Rep.* **5**, 1–11 (2016).
- Wilson, M. E. J. & Bosence, D. W. J. The Tertiary evolution of South Sulawesi: a record in redeposited carbonates of the Tonasa Limestone Formation. *Geol. Soc. London, Spec. Publ.* **106**, 365–389 (1996).
- Cannon, C. H., Harting, J., Salim, A. & Summers, M. *The vegetation of Sulawesi: Coarse Filter Analysis*. Technical Report I. (The Nature Conservancy & Texas Tech University, 2005).
- Scroxton, N. et al. Natural attrition and growth frequency variations of stalagmites in southwest Sulawesi over the past 530,000 years. *Palaeogeogr. Palaeoclimatol. Palaeoecol.* **441**, 823–833 (2015).
- Blaauw, M. & Christen, J. A. Flexible paleoclimate age-depth models using an autoregressive gamma process. *Bayesian Anal.* **6**, 457–474 (2011).

43. McKay, N. P., Emile-Geay, J. & Khider, D. geoChronR—an R package to model, analyze, and visualize age-uncertain data. *Geochronology* **3**, 149–169 (2021).

44. Bintanja, R., van de Wal, R. S. W. & Oerlemans, J. Modelled atmospheric temperatures and global sea levels over the past million years. *Nature* **437**, 125–128 (2005).

45. Schrag, D. P., Hampt, G. & Murray, D. W. Pore fluid constraints on the temperature and oxygen isotopic composition of the glacial ocean. *Science* **272**, 1930–1932 (1996).

46. Oster, J. L., Covey, A. K., Lawrence, C. R., Giannetta, M. G. & Druhan, J. L. A reactive transport approach to modeling cave seepage water chemistry II: elemental signatures. *Geochim. Cosmochim. Acta* **311**, 353–373 (2021).

47. Tooth, A. F. & Fairchild, I. J. Soil and karst aquifer hydrological controls on the geochemical evolution of speleothem-forming drip waters, Crag Cave, southwest Ireland. *J. Hydrol.* **273**, 51–68 (2003).

48. Baldini, J. U. L., McDermott, F. & Fairchild, I. J. Spatial variability in cave drip water hydrochemistry: Implications for stalagmite paleoclimate records. *Chem. Geol.* **235**, 390–404 (2006).

49. McDonald, J., Drysdale, R., Hill, D., Chisari, R. & Wong, H. The hydrochemical response of cave drip waters to sub-annual and inter-annual climate variability, Wombeyan Caves, SE Australia. *Chem. Geol.* **244**, 605–623 (2007).

50. Belli, R. et al. Investigating the hydrological significance of stalagmite geochemistry (Mg, Sr) using Sr isotope and particulate element records across the Late Glacial-to-Holocene transition. *Geochim. Cosmochim. Acta* **199**, 247–263 (2017).

51. Huang, Y. & Fairchild, I. J. Partitioning of Sr^{2+} and Mg^{2+} into calcite under karst-analogue experimental conditions. *Geochim. Cosmochim. Acta* **65**, 47–62 (2000).

52. Breecker, D. O. et al. The sources and sinks of CO_2 in caves under mixed woodland and grassland vegetation. *Geochim. Cosmochim. Acta* **96**, 230–246 (2012).

53. Breecker, D. O. Atmospheric pCO_2 control on speleothem stable carbon isotope compositions. *Earth Planet. Sci. Lett.* **458**, 58–68 (2017).

54. Basu, S., Ghosh, S. & Chattopadhyay, D. Disentangling the abiotic versus biotic controls on C_3 plant leaf carbon isotopes: Inferences from a global review. *Earth-Sci. Rev.* **222**, 103839 (2021).

55. Lagomarsino, A., Lukac, M., Godbold, D. L., Marinari, S. & De Angelis, P. Drivers of increased soil respiration in a poplar coppice exposed to elevated CO_2 . *Plant Soil* **362**, 93–106 (2013).

56. Kuzyakov, Y., Horwath, W. R., Dorodnikov, M. & Blagodatskaya, E. Review and synthesis of the effects of elevated atmospheric CO_2 on soil processes: no changes in pools, but increased fluxes and accelerated cycles. *Soil Biol. Biochem.* **128**, 66–78 (2019).

57. Covington, M. D. & Vaughn, K. A. Carbon dioxide and dissolution rate dynamics within a karst underflow-overflow system, Savoy Experimental Watershed, Arkansas, USA. *Chem. Geol.* **527**, 118689 (2019).

58. Treble, P. C. et al. Hydroclimate of the Last Glacial Maximum and deglaciation in southern Australia's arid margin interpreted from speleothem records (23–15 ka). *Clim. Past* **13**, 667–687 (2017).

59. Petit, J. R. et al. Climate and atmospheric history of the past 420,000 years from the Vostok ice core, Antarctica. *Nature* **399**, 429–436 (1999).

60. Bazin, L. et al. An optimized multi-proxy, multi-site Antarctic ice and gas orbital chronology (AICC2012): 120–800 ka. *Clim. Past* **9**, 1715–1731 (2013).

61. Jouzel, J. et al. Orbital and millennial Antarctic climate variability over the past 800,000 years. *Science* **317**, 793–796 (2007).

62. Genty, D. et al. Dead carbon in stalagmites: Carbonate bedrock paleodissolution vs. ageing of soil organic matter. Implications for ^{13}C variations in speleotherms. *Geochim. Cosmochim. Acta* **65**, 3443–3457 (2001).

63. Dorale, J. A. & Liu, Z. Limitations of Hendy test criteria in judging the paleoclimatic suitability of speleothems and the need for replication. *J. Cave Karst Stud.* **71**, 73–80 (2009).

64. Ruggieri, E. A Bayesian approach to detecting change points in climatic records. *Int. J. Climatol.* **33**, 520–528 (2012).

65. Hellstrom, J. C. & McCulloch, M. T. Multi-proxy constraints on the climatic significance of trace element records from a New Zealand speleothem. *Earth Planet. Sci. Lett.* **179**, 287–297 (2000).

66. Tadros, C. V., Treble, P. C., Baker, A., Hankin, S. & Roach, R. Cave drip water solutes in south-eastern Australia: Constraining sources, sinks and processes. *Sci. Total Environ.* **651**, 2175–2186 (2019).

67. Denniston, R. F. et al. North Atlantic forcing of millennial-scale Indo-Australian monsoon dynamics during the Last Glacial period. *Quat. Sci. Rev.* **72**, 159–168 (2013).

68. Denton, G. H. et al. The last glacial termination. *Science* **328**, 1652–1656 (2010).

69. Denton, G. H. et al. The Zealandia Switch: Ice age climate shifts viewed from Southern Hemisphere moraines. *Quat. Sci. Rev.* **257**, 106771 (2021).

70. Toggweiler, J. R., Russell, J. L. & Carson, S. R. Midlatitude westerlies, atmospheric CO_2 , and climate change during the ice ages. *Paleoceanography* **21**, 1–15 (2006).

71. Broecker, W. S. Paleocean circulation during the last deglaciation: a bipolar seesaw? *Paleoceanography* **13**, 119–121 (1998).

72. DiNezio, P. N. & Tierney, J. E. The effect of sea level on glacial Indo-Pacific climate. *Nat. Geosci.* **1823**, 1–7 (2013).

73. DiNezio, P. N. et al. The climate response of the Indo-Pacific warm pool to glacial sea level. *Paleoceanography* **31**, 1–29 (2016).

74. Du, X. et al. Deglacial trends in Indo-Pacific warm pool hydroclimate in an isotope-enabled Earth system model and implications for isotope-based paleoclimate reconstructions. *Quat. Sci. Rev.* **270**, 107188 (2021).

75. Buckingham, F. L. et al. Termination 1 millennial-scale rainfall events over the Sunda Shelf. *Geophys. Res. Lett.* **49**, 1–10 (2022).

76. Loland, M. H. et al. Evolution of tropical land temperature across the last glacial termination. *Nat. Commun.* **13**, 1–7 (2022).

77. Konecky, B. L., Noone, D. C. & Cobb, K. M. The influence of competing hydroclimate processes on stable isotope ratios in tropical rainfall. *Geophys. Res. Lett.* **46**, 1622–1633 (2019).

78. Falster, G., Konecky, B., Madhavan, M., Stevenson, S. & Coats, S. Imprint of the Pacific Walker circulation in global precipitation $\delta^{18}\text{O}$. *J. Clim.* **34**, 8579–8597 (2021).

79. Gagan, M. K., Chivas, A. R. & Isdale, P. J. High-resolution isotopic records from corals using ocean temperature and mass-spawning chronometers. *Earth Planet. Sci. Lett.* **121**, 549–558 (1994).

80. Shen, C.-C. et al. Uranium and thorium isotopic and concentration measurements by magnetic sector inductively coupled plasma mass spectrometry. *Chem. Geol.* **185**, 165–178 (2002).

81. Shen, C.-C. et al. High-precision and high-resolution carbonate ^{230}Th dating by MC-ICP-MS with SEM protocols. *Geochim. Cosmochim. Acta* **99**, 71–86 (2012).

82. Cheng, H. et al. Improvements in ^{230}Th dating, ^{230}Th and ^{234}U half-life values, and U–Th isotopic measurements by multi-collector inductively coupled plasma mass spectrometry. *Earth Planet. Sci. Lett.* **371–372**, 82–91 (2013).

83. Schrag, D. P. Rapid analysis of high-precision Sr/Ca ratios in corals and other marine carbonates. *Paleoceanography* **14**, 97–102 (1999).

84. Hathorne, E. C. et al. Interlaboratory study for coral Sr/Ca and other element/Ca ratio measurements. *Geochem. Geophys. Geosyst.* **14**, 3730–3750 (2013).

85. Partin, J. W., Cobb, K. M., Adkins, J. F., Tuen, A. A. & Clark, B. Trace metal and carbon isotopic variations in cave dripwater and stalagmite geochemistry from northern Borneo. *Geochem. Geophys. Geosyst.* **14**, 3567–3585 (2013).

86. Fick, S. E. & Hijmans, R. J. WorldClim 2: new 1-km spatial resolution climate surfaces for global land areas. *Int. J. Climatol.* **37**, 4302–4315 (2017).

87. EuroGeographics & UN-FAO. Countries, 2020—Administrative Units—Dataset. *Geoportal of the European Commission—EUROSTAT* <https://ec.europa.eu/eurostat/web/gisco/geodata/reference-data/administrative-units-statistical-units/countries> (2020).

88. Lea, D. W., Pak, D. K. & Spero, H. J. Climate impact of Late Quaternary equatorial Pacific sea surface temperature variations. *Science* **289**, 1719–1724 (2000).

89. de Garidel-Thoron, T., Rosenthal, Y., Bassinot, F. & Beaufort, L. Stable sea surface temperatures in the western Pacific warm pool over the past 1.75 million years. *Nature* **433**, 294–298 (2005).

90. Spratt, R. M. & Lisiecki, L. E. A Late Pleistocene sea level stack. *Clim. Past* **12**, 1079–1092 (2016).

91. Wang, Y.-J. et al. A high-resolution absolute-dated late Pleistocene monsoon record from Hulu Cave, China. *Science* **294**, 2345–2348 (2001).

92. Dykoski, C. et al. A high-resolution, absolute-dated Holocene and deglacial Asian monsoon record from Dongge Cave, China. *Earth Planet. Sci. Lett.* **233**, 71–86 (2005).

93. Wang, Y. et al. Millennial- and orbital-scale changes in the East Asian monsoon over the past 224,000 years. *Nature* **451**, 1090–1093 (2008).

94. Laskar, J. et al. A long-term numerical solution for the insolation quantities of the Earth. *Astron. Astrophys.* **428**, 261–285 (2004).

Acknowledgements

The project was carried out in Indonesia with permission to collect samples granted under Kementerian Negara Riset dan Teknologi (RISTEK) research permit numbers 04/TKPIPA/FRP/SM/IV/2009, 1b/TKPIPA/FRP/SM/I/2011 and 1889/TKPIPA/FRP/SM/V/2013. We thank the Research Center for Geotecnology, Indonesian Institute of Sciences (LIPI) for logistical support and are indebted to Baharudin (of Konservasi Sumber Daya Alam) and the staff of Bantimurung-Bulusaraung National Park (with special thanks to Syaiful Fajrin). Engkos Kosasih, Djupriono, Neil Anderson, Dan Zwart, Garry Smith, Linda Ayliffe, Nick Scroxton, Joel Zwart and Daniel Becker provided invaluable technical assistance in the field. We also thank Linda McMorrow, Joan Cowley, Heather Scott-Gagan, Joe Cali, Katharine Grant, Daniel Becker, and Hailong Sun for laboratory assistance. We thank Pauline Treble for informative discussions around speleothem

morphology, trace element incorporation, and conceptual models of drip pathways. This study was supported by Australian Research Council *Discovery* Project grants DP0663274, DP1095673, DP110101161, and DP180103762 to M.K.G., W.S.H., R.L.E., H.C. and C.-C.S.; an Australian Postgraduate Award and International Postgraduate Research Scholarship to A.K.K.; Science Vanguard Research Program of the Ministry of Science and Technology (110-2123-M-002-009), the Higher Education Sprout Project of the Ministry of Education, Taiwan, ROC (110L901001), and National Taiwan University (110L8907) to C.-C.S.; U.S. National Science Foundation grants (2202913) and (1702816) to R.L.E. and H.C.; and National Natural Science Foundation of China grants to H.C. (NSFC 41731174 and NSFC 41888101).

Author contributions

A.K.K. and M.K.G. designed the project; M.K.G. conceived the project; G.B.D., B.W.S., M.K.G., H.R., A.K.K., and W.S.H. performed the fieldwork; C.-C.S., H.-M.H., H.C. and R.L.E. carried out the reconnaissance and sample U-Th dating, with C.-C.S. and H.-M.H. carrying out a substantial portion of the reconnaissance dating for effective stalagmite selection; A.K.K. carried out the laboratory work and data analysis. A.K.K. wrote the manuscript with draft reviews from M.K.G. and input from all co-authors.

Competing interests

The authors declare no competing interests.

Additional information

Supplementary information The online version contains supplementary material available at <https://doi.org/10.1038/s43247-023-00873-8>.

Correspondence and requests for materials should be addressed to Alena K. Kimbrough.

Peer review information *Communications Earth & Environment* thanks the other, anonymous, reviewer(s) for their contribution to the peer review of this work. Primary Handling Editors: Yama Dixit and Joe Aslin. A peer review file is available.

Reprints and permission information is available at <http://www.nature.com/reprints>

Publisher's note Springer Nature remains neutral with regard to jurisdictional claims in published maps and institutional affiliations.



Open Access This article is licensed under a Creative Commons Attribution 4.0 International License, which permits use, sharing, adaptation, distribution and reproduction in any medium or format, as long as you give appropriate credit to the original author(s) and the source, provide a link to the Creative Commons license, and indicate if changes were made. The images or other third party material in this article are included in the article's Creative Commons license, unless indicated otherwise in a credit line to the material. If material is not included in the article's Creative Commons license and your intended use is not permitted by statutory regulation or exceeds the permitted use, you will need to obtain permission directly from the copyright holder. To view a copy of this license, visit <http://creativecommons.org/licenses/by/4.0/>.

© The Author(s) 2023